Reactions of ^{20}Ne with ^{12}C

D. Shapira, J. L. C. Ford, Jr., and J. Gomez del Campo
Oak Ridge National Laboratory, Oak Ridge, Tennessee 37830
(Received 26 March 1982)

All reaction products with $Z \geq 5$ emitted from the bombardment of ^{12}C by ^{20}Ne beams with incident energies between 54 and 80 MeV have been measured over a wide range of exit energies and angles. The quasielastic, strongly damped, and complete fusion processes were studied. At forward angles both the elastic and inelastic data show the effect of strong volume absorption. At larger angles the paucity in open direct channels manifests itself by a resonantlike behavior of the excitation functions for all outgoing channels reminiscent to that observed for $^{16}O+^{16}O$. The energy dependence of the cross section for complete fusion also shows structure, but the average magnitude of the $^{20}Ne+^{12}C$ fusion cross section is 1100 mb compared to 900 mb for $^{16}O+^{16}O$. At backward angles the $^{20}Ne+^{12}C$ quasielastic angular distribution and excitation functions show the same characteristics seen in heavier systems (e.g., $^{28}Si+^{12}C$). However, a much larger yield exists for transitions to high excitation energies (large negative Q values). This strongly damped process has a large cross section and shows all the characteristics of a long lived orbiting $^{20}Ne+^{12}C$ dinuclear system.

[NUCLEAR REACTIONS $^{20}Ne+^{12}C$, $E_{lab}=54-81$ MeV: measured forward and backward angle elastic and inelastic scattering, measured reaction products for $Z \geq 5$ at forward angles; measured $\sigma(\theta)$; strong absorption DWBA and Monte Carlo statistical model calculations.]

INTRODUCTION

The $^{12}C+^{20}Ne$ system, with α conjugate target and projectile, is likely to show a characteristic behavior similar to that observed in other light α-conjugate systems.[1-4] A comparison of this system with $^{16}O+^{16}O$ is of particular interest. The excitation functions measured for many outgoing channels of the $^{16}O+^{16}O$ induced reaction show marked broad structure characteristic of single particle states of the nucleus-nucleus potential system as well as structure of intermediate width, which is several times the average level width expected for the compound nucleus formed in the collision. Both the $^{12}C+^{20}Ne$ and $^{16}O+^{16}O$ reactions populate similar regions of excitation energy and angular momentum in the same compound nucleus; therefore, any aspects of $^{16}O+^{16}O$ behavior dictated by level density or structure of the compound nucleus should manifest themselves in $^{12}C+^{20}Ne$ reaction channels. Several studies of $^{12}C+^{20}Ne$ which address this question have already been reported[5-11] but the results so far are not conclusive. Studies of elastic scattering in Ref. 5, for example, show a marked difference between $^{16}O+^{16}O$ and $^{12}C+^{20}Ne$. In a similar study (Ref. 7), however, the $^{12}C+^{20}Ne$ elastic scattering excitation function measured at 90° c.m., where only even partial waves contribute to scattering in both systems, is very similar in character to that of $^{16}O+^{16}O$ (see Fig. 2 of Ref. 7). An additional reason for our interest in $^{12}C+^{20}Ne$ is the considerable target-projectile mass asymmetry. This system forms a link between the thoroughly investigated resonances in systems like $^{12}C+^{12}C$ and $^{12}C+^{16}O$ (Ref. 1) and the newly observed backward angle resonances in collisions between ^{12}C (or ^{16}O) and various s-d shell nuclei.[12,13]

In our study of $^{12}C+^{20}Ne$ we scanned a large portion of the total reaction yield. All emerging particles heavier than $Z=4$ were identified (Z identification) and the measurements were done over a large range of angles and energies of the outgoing products. Because of the coarse energy resolution in our experiment ($\sim$0.3 MeV c.m.) only structures broader than a few hundred keV (c.m.) could be studied. However, as a direct result of our approach, which consisted of inclusive measurements of many channels, we were able to differentiate between structure that appears only in a select few channels and the structure that appears correlated in a large number of channels. We have also measured excitation functions for elastic and inelastic scattering at backward angles. The elastic and low lying excited states show the same behavior as seen

for $^{12}C+^{28}Si$ or $^{12}C+^{24}Mg$ (Ref. 14) reactions, but our study of the full excitation energy range reveals that these low lying states are a small part of a mechanism with a large yield which we attribute to a general orbiting process.[15] Our measurements of $^{12}C+^{20}Ne$ evaporation residues yield an energy dependence which differs both in magnitude and character from that of Ref. 11; we shall comment on this result later on.

EXPERIMENTAL PROCEDURE

Energy analyzed beams of $^{20}Ne^{4+}$ from the Oak Ridge Isochronous Cyclotron were used to bombard a natural carbon foil, of areal thickness 100 $\mu g/cm^2$, at 20 bombarding energies covering the range 54 MeV $\leq E_{Ne} \leq$ 81 MeV. The experimental arrangement is shown in Fig. 1. The monitor shown is elevated 15° out of the reaction plane. Reaction products with $Z \geq 5$ were detected and identified with a position sensitive ΔE-E telescope.[16] Figure 2 shows a full ΔE-E map recorded at one of the nine angles subtended by this detector system. On the opposite side of the beam a position sensitive solid state detector preceded by a hydrogen gas absorber was used to study the recoiling carbon nuclei at five angles simultaneously. The gas pressure was adjusted at each bombarding energy so that the Ne beam and heavier particles were stopped in the foil and gas combination but the recoiling carbon ions were transmitted. The two groups that correspond to scattering to the ground and first excited states of $^{12}C+^{20}Ne$ are clearly visible in the two dimensional energy versus position spectrum shown in Fig. 3. By comparing such data to measurements done with the ΔE-E telescope at overlapping angles we were able to verify our identification of these groups. During most of the measurements the two detector systems were kept at fixed angles. The ΔE-E telescope covered the angle range $13° \leq \theta \leq 22°$ and the five-slit position sensitive detector plus absorber system covered the range from 2°—10°. At a few selected energies, however, the detectors were moved and data were taken at several angle settings scanning a larger angular range (5°—30° for the ΔE-E system).

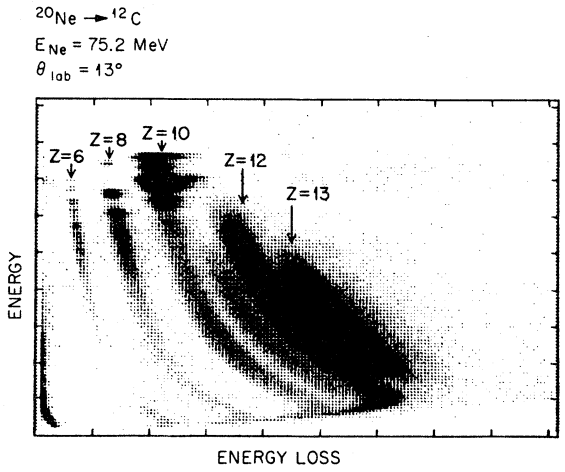

FIG. 2. A two-dimensional spectrum recorded at one of the nine angles subtended by the position sensitive ΔE-E counter used to measure the direct reaction products and evaporation residues.

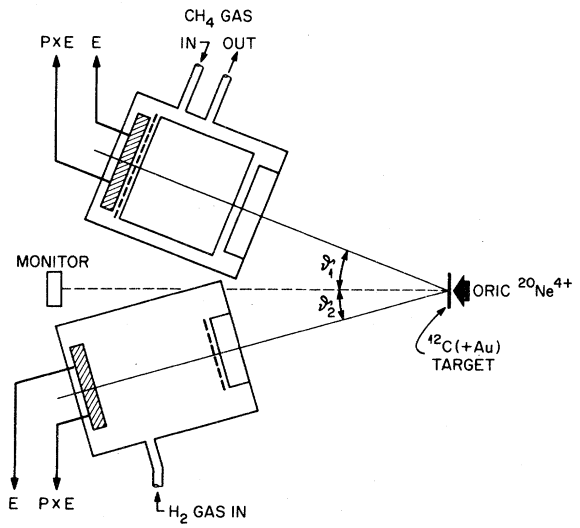

FIG. 1. A schematic of the experimental setup.

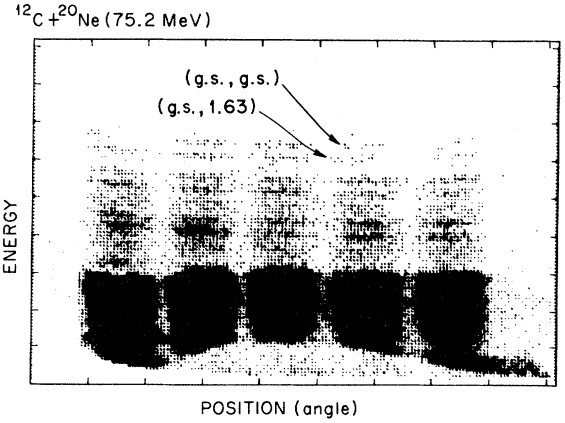

FIG. 3. An energy versus position spectrum recorded in the detector plus absorber system used to observe the recoil carbon ions. Groups corresponding to scattering to the ground and first excited states of $^{12}C + ^{20}Ne$ are indicated.

Scattering of the Ne beam from a thin (<1 μg/cm^2) gold layer deposited on the target was used to obtain an absolute normalization of the data. The ratio of gold to carbon nuclei in the target was determined by the scattering of low energy ^{14}N ions from the target. The target thickness was also determined by measuring the energy loss of 5.8 MeV α particles traversing the target. Both measurements were done after the experiment was completed and were repeated several times; each time a different location across the whole target area was scanned. The target nonuniformities measured in this way were found to be less than 10%. This observed nonuniformity is also the upper limit we place on carbon buildup on the target during the experiment. Some parts of the data were also remeasured with the same target at a later date using the integral charge of the beam collected in a Faraday cup to normalize the cross section.

The large amount of data collected will be presented in three parts. First we shall present the results of our backward angle measurements (i.e., targetlike products detected at forward angles). This will be followed by the evaporation residue, elastic, inelastic, and total reaction cross section data, and finally data on some other channels measured will be presented.

SCATTERING AT BACKWARD ANGLES

Figure 4 shows a "partially-integrated" cross section for the elastic and two inelastic transitions plotted as a function of bombarding energy. The integration is performed over five data points covering the angular interval $159° \leq \theta_{\text{c.m.}} \leq 175°$. The summation procedure used was

$$\Delta\sigma = \sum_{i=1}^{5} \frac{d\sigma}{d\Omega}(\theta_i) \sin\theta_i \, \Delta\theta_i \ . \tag{1}$$

While not all the structure seen in the individual excitation functions lines up, there is a clear similarity of these excitation functions, indicating that a large degree of cross correlation does exist.

More extensive angular distributions were measured at three energies; namely, 72.6, 74.0, and 75.2 MeV. The angular distributions measured for the ground state transition are displayed in Fig. 5. Drawn in this same figure are values of the squares of Legendre polynomials that were found to provide the closest description of the data (chosen only from a subset of Legendre polynomials of different order). One should note that two Legendre polynomials of order $L-1$ and $L+1$ could combine to approximate a polynomial of order L. Therefore the $L=14$ or 16 difference is not very significant, especially since a single Legendre polynomial does not provide a complete description of the data. The sudden transition to $L=19$ at 75.2 MeV, however, is meaningful and is also strongly favored by the fit to the data [Fig. 5(a)]. These results raise a few questions: (a) Inasmuch as these angular distributions reflect the dominance of a particular partial wave in the transition, we see that the variation with energy is neither smooth nor monotonic as one would expect if only grazing partial waves were involved. (b) The value of the maximum (critical) angular momentum for which compound nucleus formation is allowed, at this energy, is approximately $J_{\text{cr}}=19$. This value was determined from our measured evaporation residue data using a sharp cutoff approximation.[17] The dominance of partial waves as low as $L=14$ or 16 in the elastic scattering then suggests that the yield shown is due to a compound

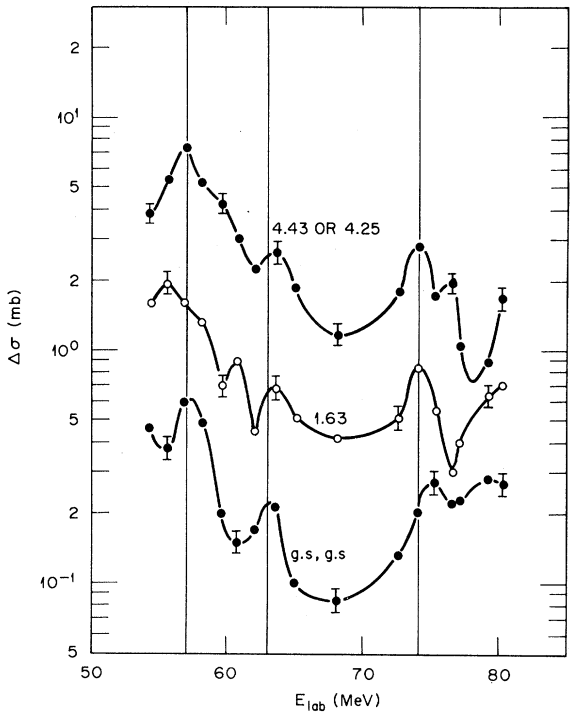

FIG. 4. Excitation functions for the elastic scattering and two inelastic transitions due to ^{12}C + ^{20}Ne collisions. The data are integrated over the angular range $159° \leq \theta_{\text{c.m.}} \leq 175°$, subtended by the detector system. Vertical lines indicate the energies at which correlated structures were observed in various exit channels.

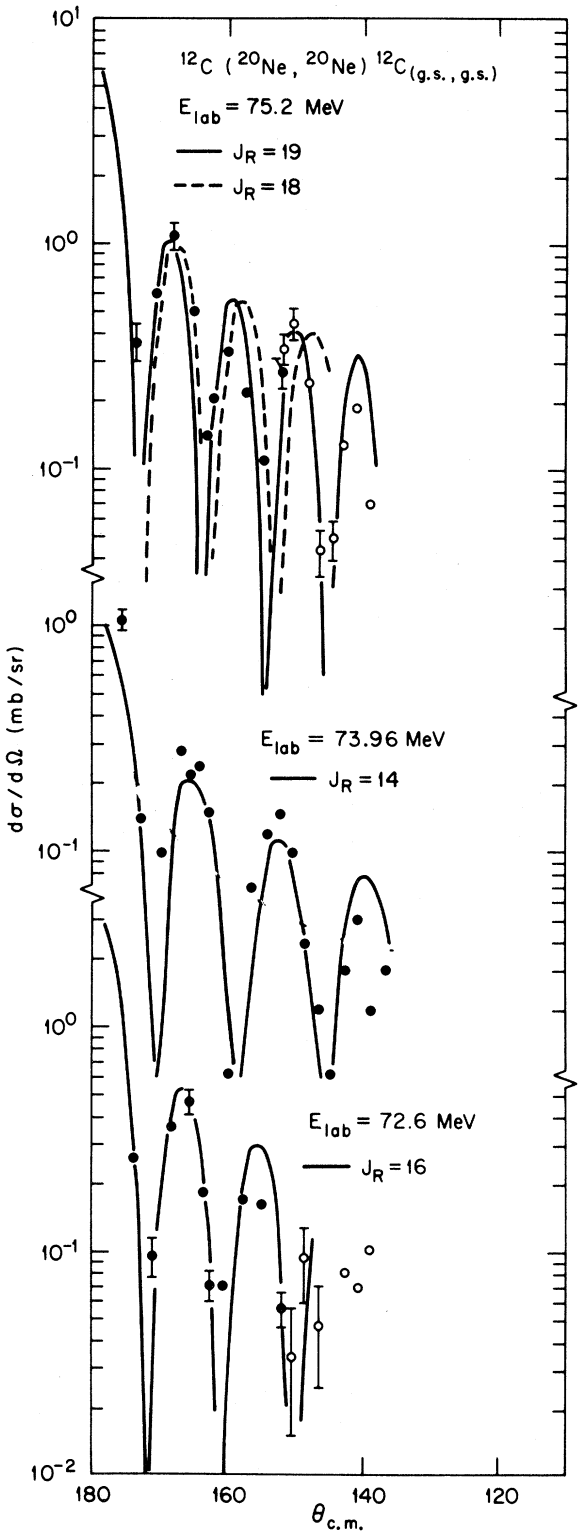

FIG. 5. The angular distributions for elastic scattering. The curves are fits to the data with Legendre polynomials of the indicated orders.

elastic process. Attempts to account for the measured back-angle cross section with a Hauser-Feshbach calculation (statistical compound nucleus) have failed to account for the large magnitude of the ^{12}C+^{20}Ne elastic cross section.[15] One should note here that the energy at which an $L=14$ angular distribution is observed ($E=74$ MeV) corresponds to a peak correlated among many outgoing channels, including the evaporation residues. We have also ascertained that the structure seen in the data of Fig. 4 has not been introduced by our sampling technique [five angles at 4° (c.m.) intervals]. Figure 6 shows the outcome of a similar sampling of artificial angular distributions dominated by single partial waves (L). Clearly the variation of the dominant L from 14 to 20 cannot introduce significant structure in our measured sample. The fact still remains then that a study of angular distributions and excitation functions measured for individual low lying transitions at backward angles did not clarify the causes underlying the behavior of the cross section at backward angles in this system.

Such irregular "spin sequences" have also been observed in other back angle data[12] where a similar experimental approach has been taken. In the present attempt to understand these phenomena we have tried to acquire a larger data base at backward angles—but instead of acquiring more detailed data on the elastic scattering we have opted to study the whole spectrum of outgoing targetlike products at forward angles. Our results have shown that the backward angle cross section rise occurs for all the inelastic data. This larger body of data on back-

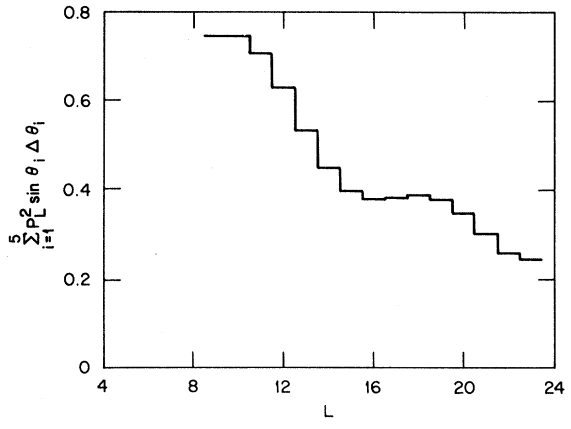

FIG. 6. A sampling of a sum of Legendre polynomials over the angular range where the excitation functions were measured. The smooth variation of the sum with L indicates that the angular range used does not artificially introduce structure into the measurements.

ward angle inelastic scattering provides information on the mechanism responsible for the increase in cross sections observed for inelastic and elastic scattering at backward angles. The mechanism which we propose, to account for the observed behavior, is orbiting—not of a single partial wave—but a more generalized phenomenon involving a wide band of partial waves (mostly, but not exclusively, from partial waves ranging between those corresponding to the strong absorption and the grazing angular momentum limits). Such a mechanism has been proposed[18] to explain the phenomenon of deep inelastic scattering (negative angle scattering) observed in heavier systems. We have already discussed this model in an earlier publication,[15] so we shall describe here briefly the evidence supporting it.

An examination of Figs. 2 and 3 shows, at a glance, that there is a yield of highly excited C+Ne inelastic products which greatly exceeds the already large cross section leading to low lying states. A full spectrum of recoiling carbon ions (obtained with the ΔE-E detector system) is presented in Fig. 7. Most of the C yield seen in that spectrum is expected to be due to the $^{12}C+^{20}Ne$ channel (thresholds for other processes are indicated in the figure).

Assuming that the observed yield originates in a $^{12}C+^{20}Ne$ two body process, then a definite reaction Q value can be associated with the outgoing C energy. The centroid of the energy distribution (a broad bump) then corresponds to the most probable Q value for that process ($\bar{Q}$). Similar spectra are observed at different angles in the backward hemisphere ($120° \leq \theta_{c.m.} \leq 180°$), and Fig. 8 shows the most probable Q value derived from C spectra measured at several scattering angles for a single bombarding energy. $\bar{Q}$ clearly stays constant over the angular range studied here, since the small deviations seen may be a consequence of angular dependencies of individual transitions, and consequently it appears that the data are consistent with one single two-body and strongly damped process. Treating the total C yield as a single process we are able to study its angle and energy dependence. Figure 9 shows the center of mass angular distribution for the total carbon yield. This $1/\sin\theta_{c.m.}$ shape of the angular distribution is characteristic of the total C yield over the whole bombarding energy range measured. Using this angular distribution the bombarding energy dependence of the integrated cross section for the total carbon yield shown in Fig. 10 is derived. We shall comment on the structure in this excitation function later but wish to note here the large magnitude of this cross section which reaches about 5% of the total reaction cross section at the highest bombarding energy measured and is still increasing.

Figure 11 shows the bombarding energy dependence of the most probable Q value. This linear relation can be expressed as

$$\bar{Q}\ (\text{MeV}) = (13 \pm 0.7) - (0.91 \pm 0.03) E_{c.m.}\ , \tag{2a}$$

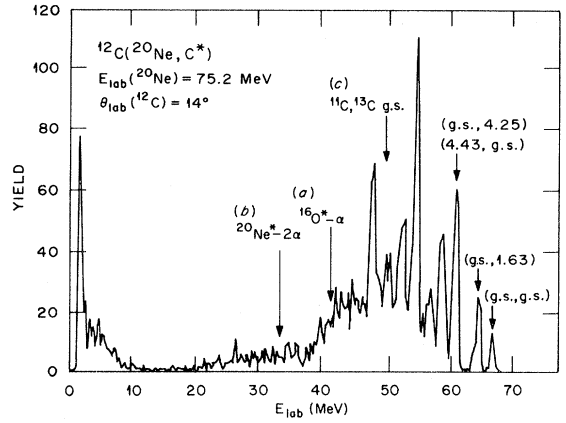

FIG. 7. Energy spectrum for outgoing carbon particles. The three arrows shown indicate the thresholds for the following processes:

(a) $^{12}C(^{20}Ne, ^{16}O^*)^{16}O \longrightarrow \alpha + ^{12}C$,

(b) $^{12}C(^{20}Ne, ^{20}Ne^*)^{12}C \longrightarrow 2\alpha + ^{12}C$,

(c) $^{12}C(^{20}Ne, ^{11}C)^{21}Ne$ and $^{12}C(^{20}Ne, ^{13}C)^{19}Ne$.

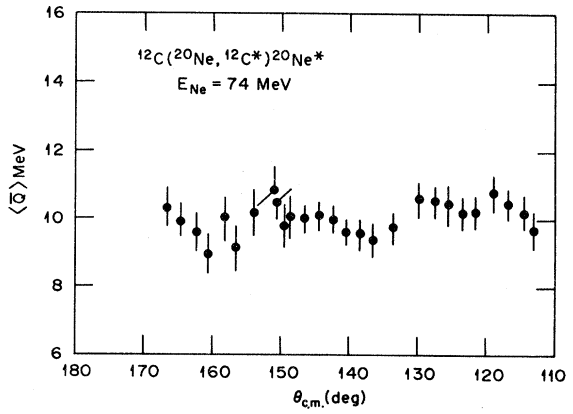

FIG. 8. The most probable Q value $\langle \bar{Q} \rangle$ obtained from carbon spectra measured at different angles at a bombarding energy of 74 MeV.

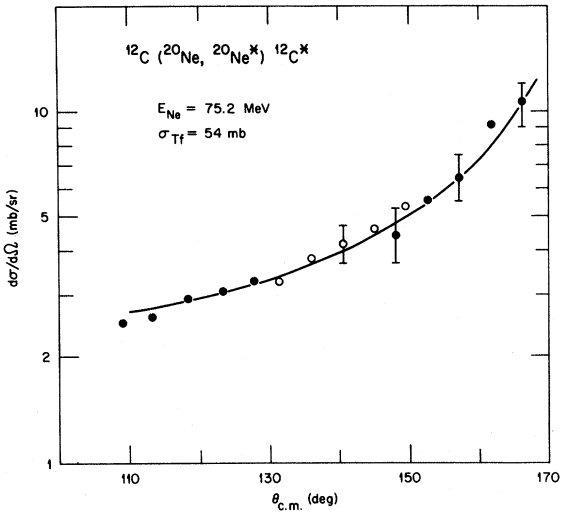

FIG. 9. The center-of-mass angular distribution for the total yield observed in the region of enhanced $^{12}C^* + ^{20}Ne^*$ events (the bump in Fig. 7). The curve is proportional to $1/\sin\theta_{c.m.}$. The open and closed circles indicate different settings of the detector system. Also indicated in the figure is the integrated yield of this fissionlike process (σ_{Tf}).

or in terms of the final kinetic energy as

$$E^f_{kin}\ (\text{MeV}) = (13 \pm 0.7) + (0.09 \pm 0.03) E_{c.m.}\ . \tag{2b}$$

To summarize the experimental results, then, we see a large inelastic yield for large negative Q values at backward angles. The angular distribution for the total yield has a $1/\sin\theta_{c.m.}$ dependence and the final kinetic energy of the outgoing (C + Ne) products is given by the linear relation (2b).

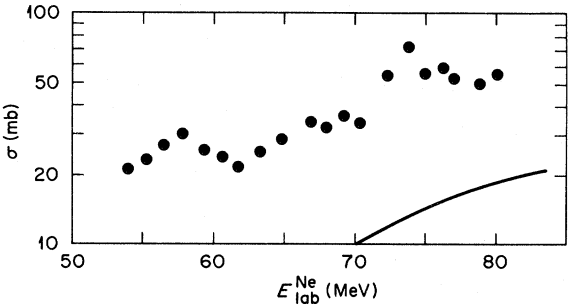

FIG. 10. The excitation function for the angle-integrated (0°—180°) yield which is illustrated in Figs. 7 and 9. Random errors are less than 8%. There is a systematic uncertainty of ±10% in absolute normalization. The solid line shows the magnitude and energy dependence predicted by the statistical evaporation model.

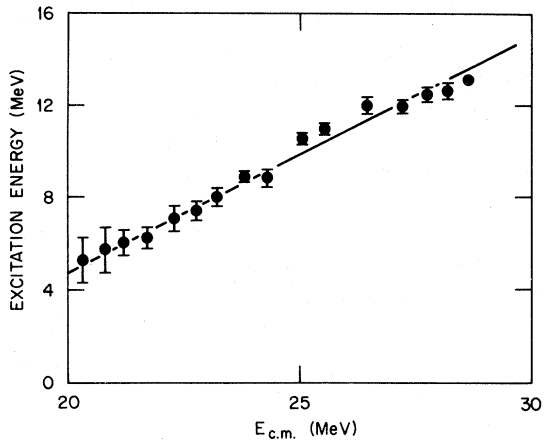

FIG. 11. The dependence of the most probable Q value on bombarding energy along with a linear fit to the data.

This behavior can be accounted for, qualitatively, with a deep-inelasticlike orbiting mechanism. The ^{12}C and ^{20}Ne form a dinuclear system that stays together and rotates long enough for a complete damping of the kinetic energy to occur. The projectile swings past 90° from its initial direction and the probability for it to separate from the target is now isotropic ($1/\sin\theta_{c.m.}$ angular distribution). The dinuclear system need survive only long enough to undergo an approximately 180° turn. This is a rather short average lifetime and one does not expect therefore any pronounced intermediate width structure to appear in the excitation function (Fig. 10). The centroid of the distribution of the kinetic energy of the products is at an energy higher than the Coulomb barrier. There clearly are contributions from the rotational energy present and these contributions are also reflected in the linear dependence of the most probable final kinetic energy on the bombarding energy (Fig. 11).

An orbiting mechanism could also account for the pronounced structure seen in the excitation functions for individual transitions. For a particular bombarding energy, favorable matching of one partial wave in the entrance channel to one in the exit channel can occur, producing an enhancement in the cross section. As the bombarding energy varies these matching conditions could change according to details of the interaction at the nuclear surface, thus producing the observed resonancelike structure. Such a critical dependence on matching conditions is especially pronounced in a situation where there is only a small number of competing open exit channels. The two dimensional ΔE-E

spectrum in Fig. 2 shows that for $Z \leq 10$ only even Z products appear—the cross sections leading to $Z=5$, 7, and 9 are negligible. Because of their unfavorable Q values these channels are virtually closed, so that essentially the only channels open for most noncompound processes are those leading to final nuclei that are α conjugate.

The importance of rotational energy contributions to the final kinetic energy of deep inelastic reaction products has been discussed by several authors[19–22] for several light heavy ion collisions ($A_{CN} \lesssim 80$). When a quantitative analysis of the energy dependence of Fig. 11 [Eq. (2b)] is attempted in the spirit suggested by the authors of these references (Refs. 19–22), some questions arise.

In that analysis the kinetic energy of the products is equated to the total barrier that the two final state nuclei experience during scission,

$$E_f^{\text{kin}} = V_f(R) + V_{\text{rot}}(R) ,$$
$$V_f(R) = V_{\text{Coul}}(R) + V_{\text{nucl}}(R) . \tag{3}$$

If we neglect the nuclear potential (Ref. 19) we have

$$E_f^{\text{kin}} = 1.44\frac{Z_1 Z_2}{R} + 20.9 f^2 \frac{l_i(l_i+1)}{\mu R^2} , \tag{4a}$$

where $Fl_i = l_F$, l_i is the initial angular momentum, and l_f is the angular momentum in relative motion of the final state. If the nuclear interaction potential is included, according to the prescription given in Ref. 21, we get for

$$^{12}\text{C} + ^{20}\text{N} \rightarrow ^{12}\text{C}^* + ^{20}\text{Ne}^* ,$$
$$E_f^{\text{kin}} = 1.44\frac{Z_1 Z_2}{R_c} + (1-f^2)V_{\text{nucl}}(R_{\text{cr}}) + f^2 E_{\text{c.m.}} , \tag{4b}$$

where the scission radius is R_{cr} which is the critical distance for fusion, and $V_{\text{nucl}}(R_{\text{cr}})$ is the critical potential at R_{cr}. Equating (4a) and (2b), we obtain by setting $l_f = 0$ as $E_f \rightarrow V_{\text{Coul}}$,

$$R = 6.65 \pm 0.35 \quad (r_0 = 1.33 \pm 0.6 \text{ fm})$$

TABLE I. Angular momenta cutoff values.

E_{NE}	J_{cr}[a]	J_{SA}[b]	J_{gr}[c]
54.2	15	15	15
60.7	16	16–17	17
68.1	18	18	19
75.2	19	19–20	21
80.2	19–20	20–21	22

[a]Critical angular momentum limit for fusion as obtained from evaporation residue data and the sharp cutoff approximation.
[b]Orbital angular momentum at the strong absorption radius [Eq. (5)].
[c]Grazing angular momentum is defined as the angular momentum for which the optical model transmission coefficient has the value $\eta_l = 0.5$. The optical potential parameters used are from Refs. 5 and 6.

and

$$f^2 \frac{d}{dE_{\text{c.m.}}}[l_i(l_i+1)] = 1.43 \pm 0.48 .$$

Taking l_i along the critical angular momentum trajectory obtained from our fusion data (see Table I), we get

$$f = 0.28 \pm 0.16 ,$$

i.e., on the average only 30% of the orbital angular momentum in the entrance channel is present in the damped exit channel. This reduction is in excess of expectations based on the classical sticking limit.[20] What is more troublesome is the fact that such a reduction in orbital angular momentum mandates that the outgoing fragments carry 70% of the incoming angular momentum in the spins of their excited states. If we take, for example, the data at $E_{\text{c.m.}} = 28$ MeV (75.2 MeV Ne) and use the value of the critical angular momentum for fusion in the entrance channel (see the next section and Table II) $J_{\text{cr}} = 19$, then we conclude that $^{12}\text{C}^* + ^{20}\text{Ne}^*$ must carry a combined spin of 12 or 13. At an average excitation energy of 12 MeV (Fig. 11) no states of such high spin are available in either nuclei. The

TABLE II. Total reaction cross sections.

$E_{\text{c.m.}}$	σ_f	σ_{DR}	σ_R	σ_R(OM)[a]	σ_R(OM)[b]
22.1	1100±100	400±60	1500±160	1370	1490
28.1	1250±110	360±60	1610±160	1540	1800

[a]Parameters from Refs. 5 and 6. Real part: $V_R = 17$, $r_0^R = 1.35$, and $a_R = 0.57$. Imaginary part: $V_I = 1 + 0.54E_{\text{c.m.}}$, $r_0^I = 1.35$, and $a_I = 0.57$.
[b]Parameters from Ref. 7. Real part: $V_R = 17$, $r_0 = 1.35$, and $a_R = 0.49$. Imaginary part: $V_I = 0.8 + 0.2E_{\text{c.m.}}$, $r_0^I = 1.27$, and $a_I = 0.15$. Surface imaginary: $V_{IS} = -0.31 \pm 0.003E_{\text{c.m.}}^2$, $r_0^{IS} = 1.45$, and $a_{IS} = 0.805$.

reason for this inconsistency is not clear. Trying to work with the Coulomb plus nuclear interaction (Ref. 21) leads to a smaller radius but similar f values. The problem, then, may lie with our assumption about the incoming angular momentum trajectory. The low angular momenta that dominate the elastic scattering at backward angles (see Fig. 5) suggest that angular momenta below $l = l_{cr}$ may participate significantly in this backward angle process. It has already been suggested by several authors that partial waves lower than the critical (maximum) angular momentum leading to fusion may contribute to observed deep inelastic processes[22–24,26] as do recent light particle-heavy ion correlation data measured for $^{32}S + {}^{27}Al$ deep inelastic processes.[25]

The problem could also be due to our application of Eqs. 4(a) or (b) and the assumption made that the only source for the dependence of final kinetic energy on the bombarding energy is the centrifugal barrier. An increase in deformation of the fragments at scission could account for some of the energy dependence. During their extended time of contact the colliding nuclei could repeatedly exchange one or more α particles forming a substantial neck of nuclear matter and consequently a much lower barrier when they separate.

EVAPORATION RESIDUES

The position sensitive ΔE-E detector system was used to identify all the outgoing reaction products with $Z > 4$. The atomic numbers of different reaction products are indicated in Fig. 2. Figure 12 shows the energy spectrum of all those products with $Z > 10$. The peak of the broad energy distribution is located at the energy corresponding to evaporation residues with the average velocity of the compound nucleus. There is also an enhanced yield at lower energies. This "shoulder" in the energy spectrum is contributed mostly by events from the $Z = 12$ group as can be seen from the two dimensional map of Fig. 2. We shall further discuss this structure later on, however at present we only note that this yield has been included in the summed evaporation residue yields. The evaporation residue yield has been measured at all the bombarding energies over the angular range $13° \leq \theta_{lab} \leq 22°$ subtended by one setting of the detector. At three bombarding energies, however, full angular distributions were measured ($5° \leq \theta_{lab} \leq 30°$). The shapes of these angular distributions measured at bombarding energies of 60.7, 74, and 75.2 MeV served as a guide

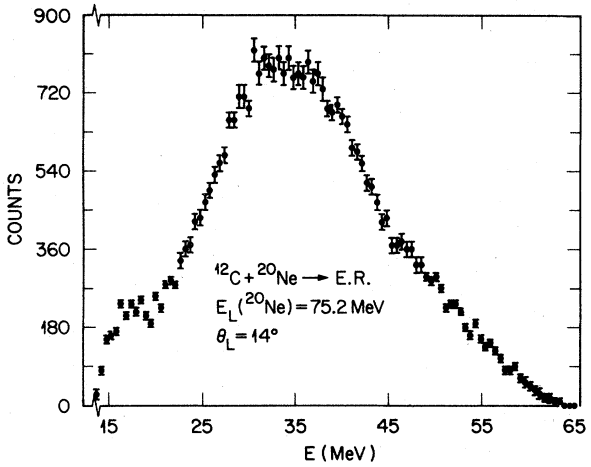

FIG. 12. An energy spectrum for all reaction products with $Z > 10$.

when "integrating" the partial angular distribution measured at other energies in order to obtain the total evaporation residue cross sections. The resulting excitation function is shown in Fig. 13 (full circles). Also shown in the same figure are the data from

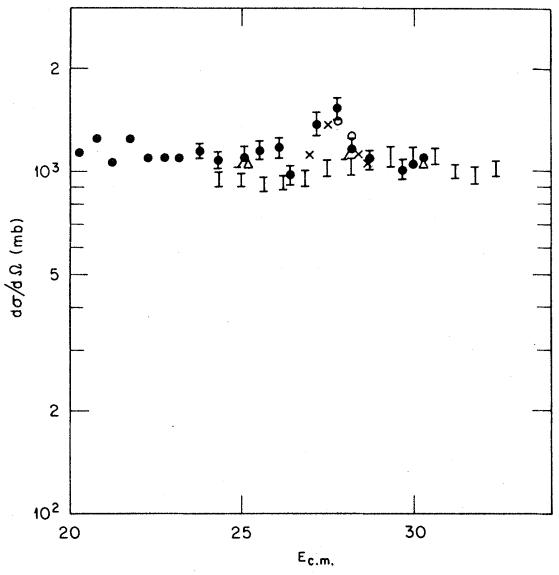

FIG. 13. The excitation function for the evaporation residues as integrated over the angular range ($13° \leq \theta_{lab} \leq 22°$) subtended by one setting of the ΔE-E detector system. The error bars indicate only estimates of relative errors from counting statistics and extrapolation. The open circles and triangles and ×'s indicate repeat measurements made to verify the magnitude and structure of the observed data. The vertical bars are the measurements of Tserruya *et al.* (Ref. 11).

Ref. 11 (shown as vertical bars) which differ qualitatively from ours. The structure that we measured around $E_{c.m.}=27$ MeV may be somewhat exaggerated because of the limited angular interval over which the data were taken. We measured full angular distributions at two of the energies in the region of this structure. They are shown in Fig. 14—also indicated in this figure is the angular range over which most of the data were taken. The integrals of the angular distributions seen in Fig. 14 are indicated in Fig. 13 by open circles and although the structure does appear to be less pronounced, it is clearly present. In a separate experiment we have remeasured the evaporation residues with the same target over a small energy range around this structure using a different normalization procedure (integrating the beam current rather than using the scattering from a gold layer). The results are displayed in Fig. 13 by $\times$'s and the structure is again reproduced. It is not obvious why our results differ from those of Ref. 11. However, there are real differences between the two measurements—in Ref. 11 all charges with $Z>6$ could be included in the evaporation residue yield since the incident beam was ^{12}C, whereas in the present measurements only $Z>10$ could be included. Also the target in Ref. 11 was natural Ne gas (i.e., $>8\%$ ^{22}Ne) while in our experiment a ^{20}Ne beam was incident on a target which was 99% ^{12}C (i.e., natural carbon).

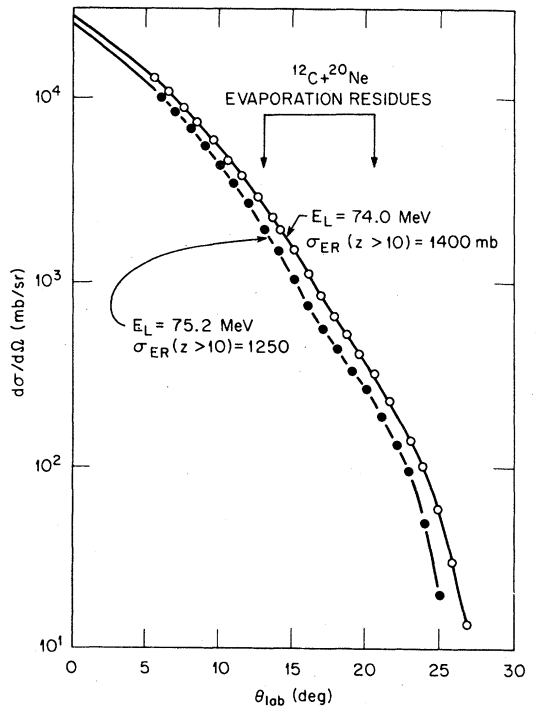

FIG. 14. The full angular distributions measured for the evaporation residues at energies just on and off the resonantlike bump seen in the excitation function of Fig. 13. The integrated cross sections from these data are shown in Fig. 13 by the open circles. The brackets indicate the range of angles subtended by the ΔE-E detector system with which the excitation function data of Fig. 13 shown as closed circles were measured.

In the study of fusion of light heavy ions some difficulty is encountered in separating products of fusion evaporation processes from those resulting from other reaction mechanisms, and the present system is no exception. To facilitate comparison with other data sets and to be specific as to what we define as fusion evaporation products, the procedure of our data analysis at one energy will be described in detail. The actual data are compared with the results of a complete kinematic simulation of the evaporation of light particles from a compound nucleus populated with the same assumed angular momentum distribution and the same excitation energy.[17,27] The measured and calculated energy spectra, angular distributions, and relative yields of different evaporation residues can be compared. Figure 15 compares measured evaporation residue angular distributions for products of four different atomic numbers with calculated distributions. The identification of the evaporation residues was simple except in the case of the $Z=12$ spectra. Magnesium spectra measured at two angles are shown in Fig. 16. The expected location of the centroid for the energy distribution of evaporation residues is indicated in the figure. There is a peak in the energy distribution at this energy, but additional groups are also present in these spectra. The location of the two peaks (labeled I and II) as a function of scattering angle can be kinematically accounted for by assuming ^8Be emission from the compound system leading to moderate excitation in the exit channel. Such ^8Be emission would have a surprisingly large yield. At this point, however, this must be considered merely a possibility because charge but not mass was identified in the experiment. Finally a comparison of measured and calculated relative yields is shown in Fig. 17. Again a discrepancy is apparent for $Z=12$. Standard parameters are used in these calculations and their values appear in the Appendix.

The kinematic Monte Carlo calculation that was used to calculate the energy spectra for α, p, and n evaporation from the compound nucleus was modified to include ^8Be emission. Artificially forcing a large first chance ^8Be emission from the compound

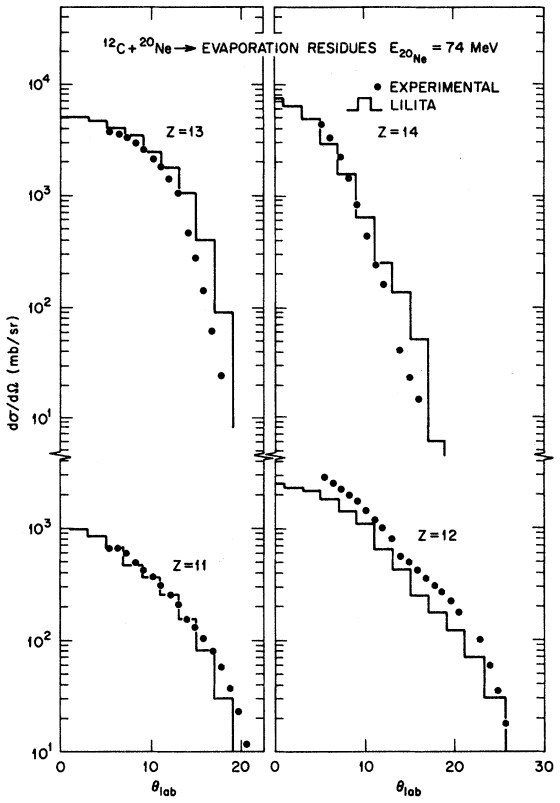

FIG. 15. Measured angular distributions for evaporation residues with different values of Z as compared with the results of Monte Carlo statistical model calculations (Ref. 27).

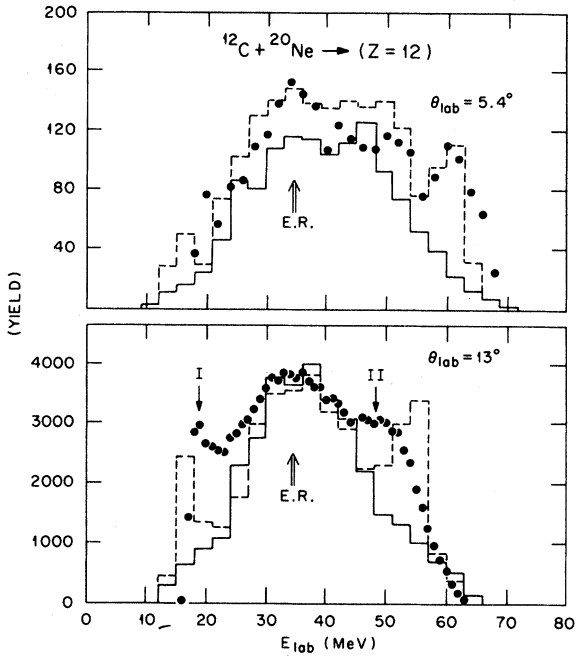

FIG. 16. Magnesium spectra measured at two angles compared with histograms calculated with the LILITA Monte Carlo code. The arrow marked ER indicates the expected location of the centroid of the energy distribution of the evaporation residues. The two peaks labeled I and II may be due to emission of ^{8}Be from the compound nucleus. Artificially including a large ^{8}Be yield from the compound nucleus in the calculations results in the spectral shape shown by the dotted lines in the figure.

system results in a spectral shape shown by the dotted line in Fig. 16. The α/Be first chance emission ratio needed to reproduce this spectral shape is 1.70 but it should be stressed here, however, that the assumed compound nuclear origin of the ^{8}Be yield is not necessitated by the data. The Be yield may originate in other reaction processes, as only the kinematic features of Be emission are used in this comparison.

OTHER REACTION CHANNELS

The detection system used made it possible to measure many other reaction products. Figure 18 shows elastic scattering and direct reaction angular distributions measured at a bombarding energy of 75.2 MeV. The direct reaction cross section shown here is derived from the sum of the inelastic yield for $Z=10$ products and all the products with $Z<10$. Extrapolating the angular distribution shown in Fig. 18 and integrating it yields the direct reaction cross section shown in Table II. The total

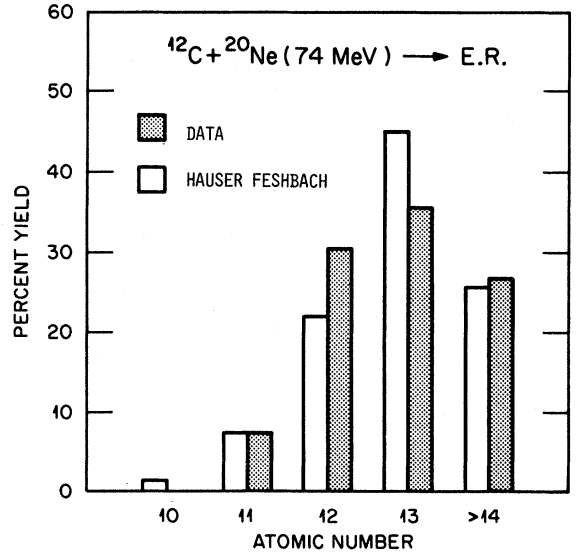

FIG. 17. The evaporation residue yields as a percentage of the total fusion cross section at a bombarding energy of 74 MeV. The solid and open bars represent the data and Monte Carlo calculations, respectively.

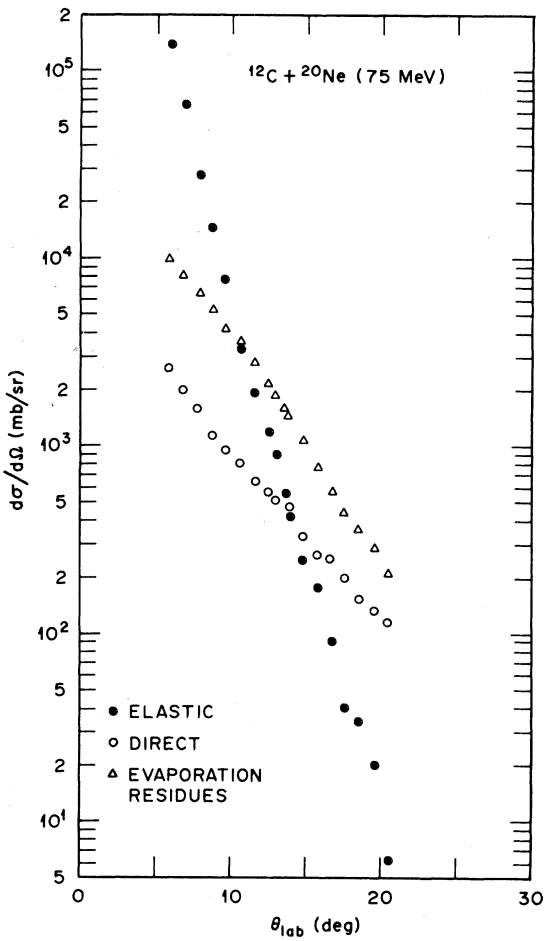

FIG. 18. The angular distribution measured at 75 MeV for the direct reaction cross section defined as the sum of the inelastic yield for $Z=10$ and all reaction products with $Z<10$. The angular distributions for the elastic scattering and evaporation residues are shown for comparison.

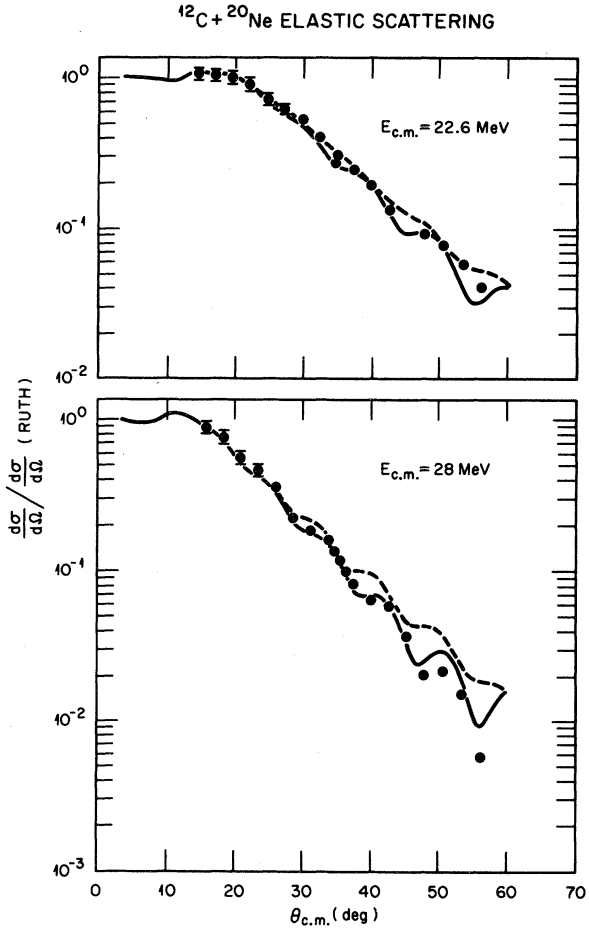

FIG. 19. The elastic scattering measured at bombarding energies of 60.7 and 75 MeV. The dashed and solid lines are optical model calculations using the parameters of Refs. 6 and 7, respectively (see Table II).

reaction cross section shown in Table II is the sum of the evaporation residue and the direct reaction cross sections. The elastic scattering data measured at 75 MeV and 60.7 MeV (laboratory) shown in Fig. 19 are described fairly well by qualitatively different sets of optical potential parameters taken from Refs. 6 and 7 (see Table II). Both potentials provide an adequate description of the rapid falloff from the Rutherford cross section, but at large angles they diverge. The potential (G) of Ref. 7 with an energy dependent surface absorption term provides a better qualitative description of the large angle data. This is done, however, at the expense of overpredicting the total reaction cross section (absorption at very large radii). The potential used in Refs. 5 and 6 on the other hand accounts correctly for the measured total reaction cross section. What this analysis suggests then is that the initial rapid falloff is due to removal of flux into a region of strong absorption (probably compound nucleus formation) with very little flux returning to the elastic channel—such absorption can be easily described using an entrance channel optical model with absorption. The variation of the elastic cross section at larger angles, past the rapid falloff region, is probably strongly affected by the coupling to other direct channels, and attempts to describe its behavior with an optical potential lead to distortions. A similar situation prevails with the inelastic data. Although coupling to other channels should be important, the inelastic data measured over the same limited angular range where the elastic data show the dominance of simple strong absorption also show the effect of a sharp-strong absorption ra-

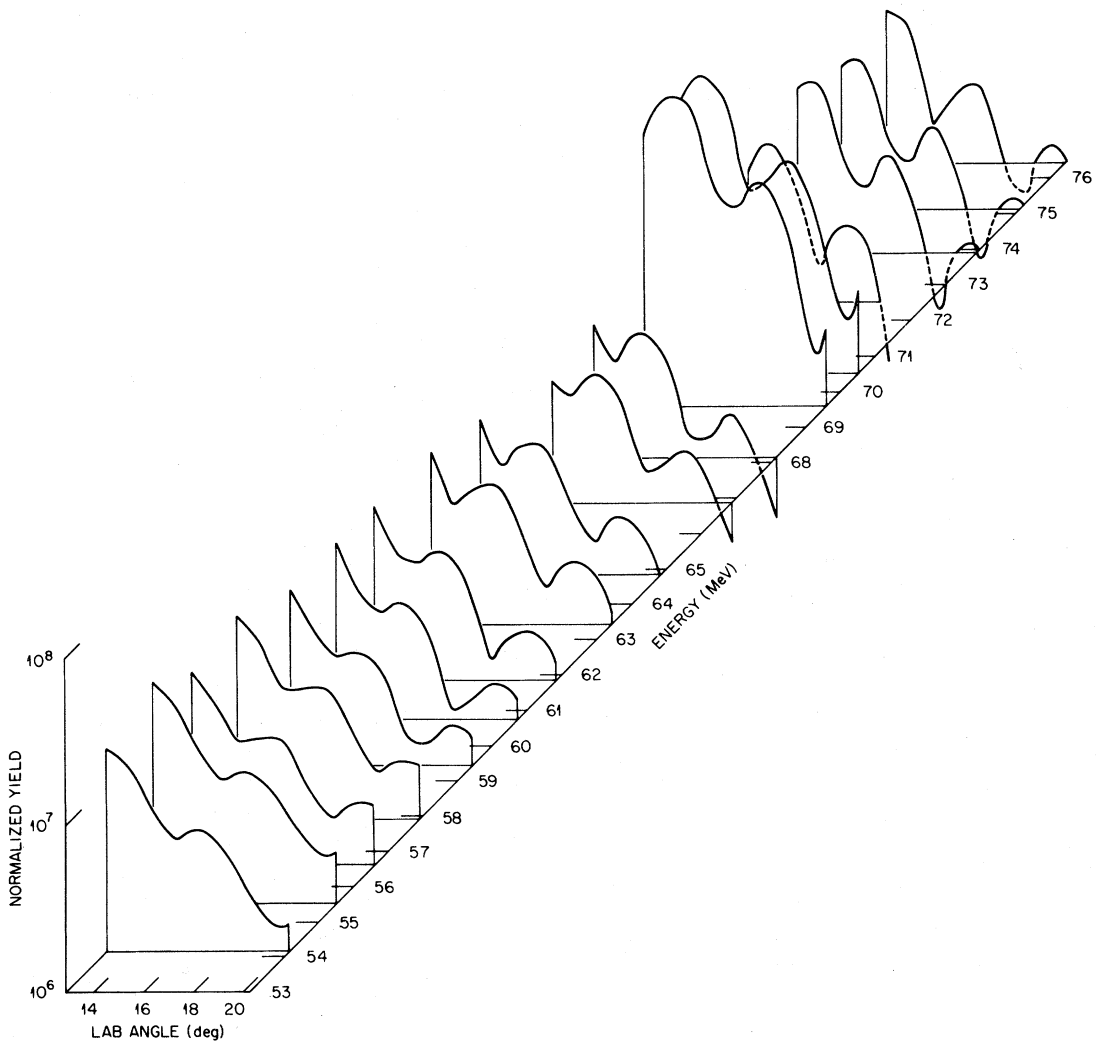

FIG. 20. Measured angular distributions for inelastic scattering to the first 2^+ state (1.63 MeV) of ^{20}Ne as a function of the incident energy.

dius. The angular distributions for the 0^+ (g.s.) to 2^+ (1.63 MeV) transition measured over the angular range $12° \leq \theta_{\text{lab}} < 23°$ between $54 \leq E_{\text{Ne}} < 80$ MeV are shown in Fig. 20. The data show oscillatory structure superposed on a general decreasing trend as θ_L increases. Visual inspection of these oscillations shows an increase in frequency and a shift toward smaller angles with increasing bombarding energy. Assuming channel coupling is minimal the data can be described using the DWBA formalism in the strong absorption limit.[28] In this limit the differential cross section is approximated by:

$$\frac{d\sigma}{d\Omega} \propto \sum_{(m,l+m \text{ even})} [l,m]^2 \, | \, Y^{-m}_{L=L_0}(\theta,0) \, |^2 , \tag{5a}$$

$$[l,m] \equiv i^l \frac{[(l-m)!(l+m)!]^{1/2}}{(l-m)!!(l+m)!!} \quad l+m \text{ even}$$

$$\equiv 0 \quad l+m \text{ odd} , \tag{5b}$$

where l is the multipolarity of the transition ($l=2$) and L_0 is the orbital angular momentum at the strong absorption radius ($\sim kR_{\text{SA}}$). We have used the above formula to describe the oscillations in the data, and Fig. 21 shows the quality of the data and fits at two energies. Figure 21(b) shows the effect when the oscillatory pattern is added to a damping exponentially decreasing background. Table I shows the orbital angular momenta (J_{SA}) deduced at several energies, along with the critical angular

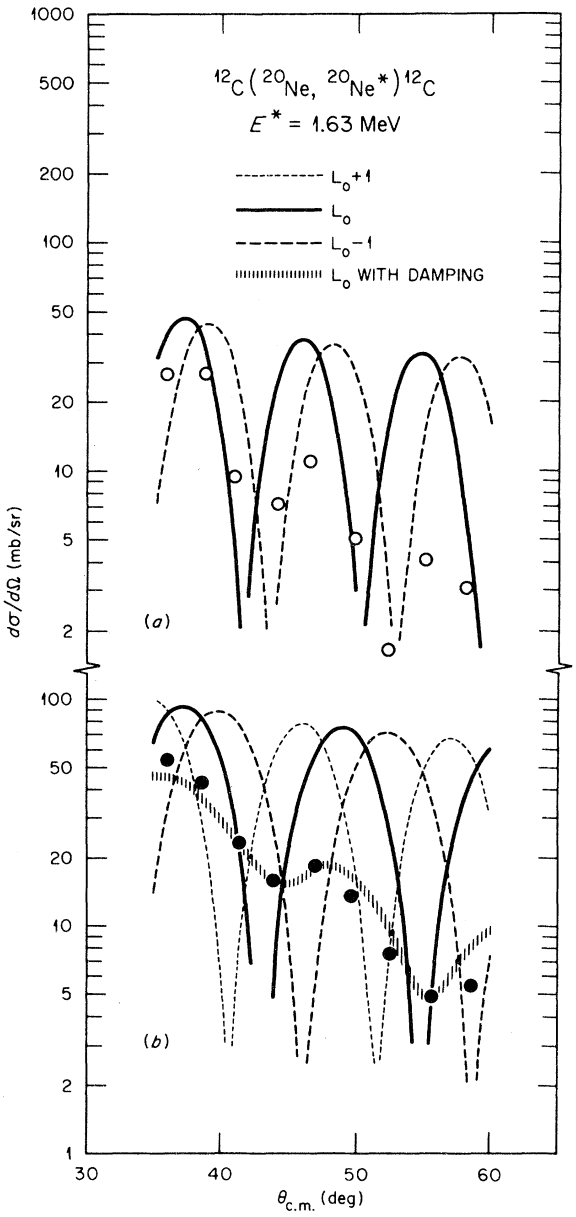

FIG. 21. Angular distributions for scattering to the 1.63 MeV state of ^{20}Ne compared with calculations using the strong absorption model. The hatched curve shows the effect of damping by adding an exponentially decreasing background to the oscillatory strong absorption curve.

momenta derived from our fusion data and the grazing angular momenta obtained with the optical model potential of Refs. 5 and 6. Note that the strongly absorbed angular momenta $l \leq L_{SA}$ are the same as those for which fusion occurs $l \leq L_{cr}$. Apparently not only the elastic but also the inelastic data in this angular region are most sensitive to flux being removed to the compound nucleus with little chance of feeding back. Clearly as one moves to larger angles and smaller cross sections the yield will be strongly affected by the effects of coupling to other channels—our analysis, therefore, only concentrates on that forward part of the inelastic angular distribution.

A marked feature of the two dimensional spectrum shown in Fig. 2 is the dominance of even Z products, especially below $Z=10$. This suggests that most of the measured $Z=6$ and 8 yield is produced by ^{12}C and ^{16}O. The carbon yield has been already discussed. On the basis of the mechanism postulated for the C production (deep inelastic scattering) one might expect other products with Z close to that of the target to exhibit similar behavior. Unfortunately $Z=5$ and 7 yields are almost nonexistent and the $Z=8$ yield has a strongly forward peaked component produced by the stripping of an α particle from the Ne projectile. A typical oxygen spectrum is shown in Fig. 22 which shows a pronounced enhancement of the yield at high excitation energies as do the C spectra, but the spectrum is dominated (particularly at forward angles) by large yields from transitions to low lying states. Figure 23 shows the angular distributions of $Z=8$ products at excitation energies below and above 8 MeV. All show a strong forward peaking in the center of mass system and large yields. Figure 24 shows excitation functions measured for different $^{12}C(^{20}Ne,^{16}O)^{16}O$ transitions (integrated over the angular interval $13° \leq \theta_{lab} \leq 22°$). There is pronounced structure in the excitation function, especially for the ground state transition. None of this structure shows a clear correlation with that observed in other excitation functions. However, the total transition strength (summed over all excitation energies) may reveal underlying structure that

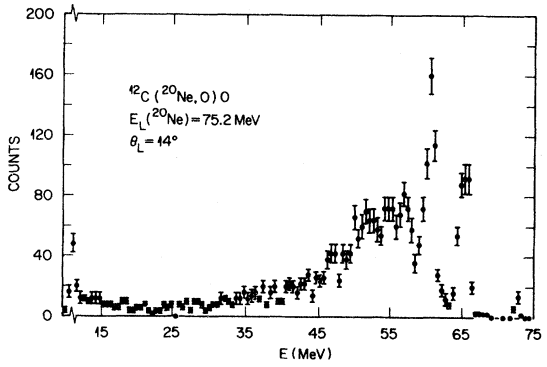

FIG. 22. The oxygen spectrum observed at an incident energy of 75.2 MeV and a laboratory angle of 14°.

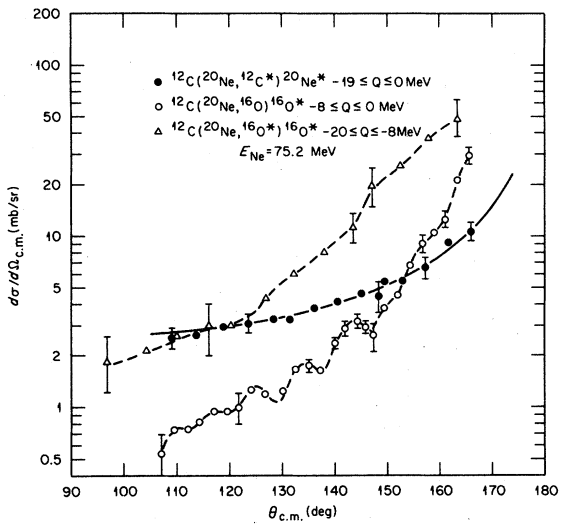

FIG. 23. Angular distributions for the oxygen yields corresponding to low and high regions of excitation energy. The summed carbon yield is shown for comparison.

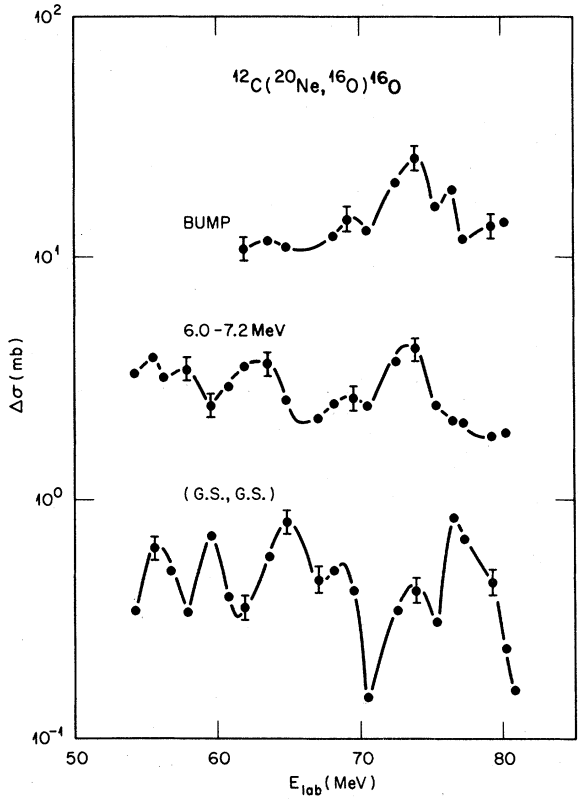

FIG. 24. Excitation functions for different energy intervals of the oxygen yield (integrated over the angular range $13° \leq \theta_{lab} \leq 22°$). The upper curve is for the main bump seen in spectra such as that of Fig. 22.

might signal the presence of a resonance in the composite system.

Figure 25 presents a summary of many outgoing channels—much of the structure seen for individual transitions is washed out but some structure does remain. The most significant enhancement is present around the bombarding energy of 74 MeV ($E_{c.m.} \sim 27.8$ MeV). The limited energy resolution of ~ 0.3 MeV and large energy steps of ~ 1.4 MeV with which the data were measured limit the determination of the total width of this structure to an

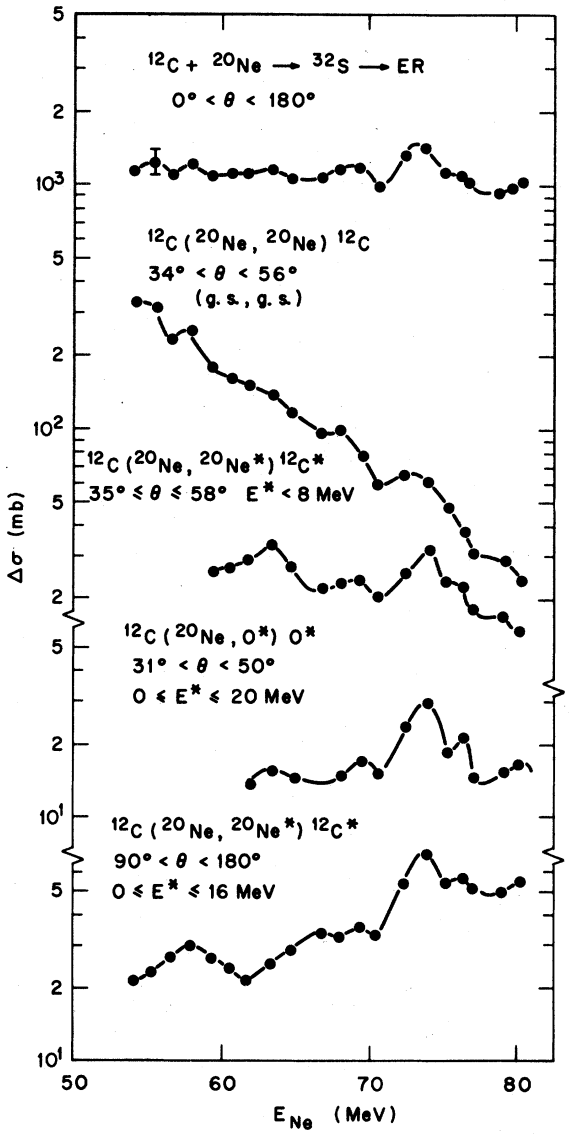

FIG. 25. A comparison of excitation functions measured for different exit channels of the ^{12}C+^{20}Ne system. The prominent peak observed near 74 MeV appears to be correlated among many of the channels.

estimate of about 1 MeV in the center of mass system. The only two processes for which we have an integrated cross section are the evaporation residues and the total C + Ne orbiting process yield (in the backward hemisphere). In both cases partial widths would not lead to reduced width (or structure information) because many transitions are involved. Determining the background is also very difficult. The data needed for such an analysis are full angular distributions for many individual transitions measured at several energies with fine resolution and these we do not possess. The data shown in Fig. 25 only serve to indicate the possible location of resonant phenomena in $^{12}C + ^{20}Ne$ induced reactions but are not sufficient to make any nuclear structure studies.

SUMMARY

Many final products from $^{12}C + ^{20}Ne$ induced reactions have been studied. That system was found to have a marked paucity of open noncompound channels (only even Z products). A study of the excitation functions for individual transitions reveals characteristics (structure) similar to those of the $^{16}O + ^{16}O$ system, in particular for the elastic, inelastic, and α transfer channels measured here. Since only a few channels are open for direct reactions the change of partial waves inside the grazing limit can drastically affect the cross section for any particular transition, and the observed structure depends on the particular matching of the reaction channel to the entrance channel at this bombarding energy. Since only even partial waves participate in the $^{16}O + ^{16}O$ reactions, the best and most relevant comparison to $^{20}Ne + ^{12}C$ data can be done at 90° c.m. where only even partial waves contribute to the observed transitions in both systems.[29]

The $^{12}C + ^{20}Ne$ fusion cross section shows structure in the excitation function that is qualitatively similar to the $^{16}O + ^{16}O$ fusion data. Most interesting is a peak in the evaporation residue cross section at $E_{c.m.} = 27.8$. The $^{16}O + ^{16}O$ evaporation residue data[30] also peak at an energy of 30 MeV which corresponds to the same excitation energy in ^{32}S. The structure in the $^{16}O + ^{16}O$ data at this particular energy is, however, broader than that seen for $^{12}C + ^{20}Ne$. Examination of many outgoing channels has shown that the structure around 27.8 MeV center of mass energy appears in most outgoing channels.

Analysis of the elastic scattering data with the measured total reaction cross section indicates that the angular region where the ratio of the elastic cross section to the Rutherford cross section begins to drop rapidly is not sensitive to coupling to other direct channels. Therefore, the most significant source of flux removal is the formation of the compound nucleus. A similar effect is seen in the inelastic data measured over the same angular range. We believe that searches for global optical model parameter sets for heavy ion scattering benefit from the approach outlined in this work.[31] The forward angle region, in which the cross section shows a rapid falloff from Rutherford scattering, is used to obtain a set of optical parameters and the measured total reaction cross section is then used to remove some of the ambiguities.

An orbiting mechanism is proposed to account for the resonant structure observed in the excitation functions for transitions to individual final states as well as the large damped (deep inelastic) yields observed in the energy spectra of the recoiling carbon nuclei. An analysis of the energy dependence of this damped component raises questions about the angular momentum of the separating fragments or their deformation at scission. Light ion-heavy ion correlation and heavy ion-heavy ion coincidence data are needed to determine the angular momentum distributions of the entry states and of the final fragments in order to further study this problem. The suggested interpretation of the $^{12}C + ^{20}Ne$ data in terms of a general orbiting mechanism could be further probed by measurements on a system with a large target-projectile asymmetry, such as, e.g., $^{28}Si + C$, where more outgoing channels can be studied at backward angles. Such measurements are now underway.

Oak Ridge National Laboratory is operated by Union Carbide Corporation under Contract W-7405-eng-26 with the U. S. Department of Energy.

APPENDIX: STATISTICAL MODEL CALCULATIONS

The statistical model calculations given in Figs. 15–17 were done with the Monte Carlo Hauser-Feshbach code LILITA.[27] This code uses the sharp cutoff approximation for the transmission coefficients at regions of high excitation energies (~20 MeV), and the transmission coefficients are calculated using the optical model parameters given by Perey and Perey.[32] The compound nucleus is allowed to deexcite only by the emission of neutrons

TABLE III. Level density parameter a used in the LILITA calculations for the fusion of ^{20}Ne+^{12}C.

Z	A[a]			a		
16	32	4.1	3.85	[b]	[b]	[b]
15	31	4.1	3.60	3.30	[b]	[b]
14	30	3.81	3.86	3.30	3.60	3.46
13	29	3.86	3.73	3.95	3.80	3.45
12	27	3.60	3.75	3.65	3.50	3.30
11	25	3.65	3.65	3.55	3.45	2.90
10	23	3.50	3.40	3.65	3.50	2.80

[a]Each row gives the value of a for each nucleus included in the calculations for the indicated value of Z and for A, $A-1$, $A-2$, $A-3$, and $A-4$.
[b]Nuclei excluded from the competition.

(n), protons (p), and α particles. The Fermi gas model level density is used with the equations given in Ref. 33 and with values of the pairing energy, Δ, also given in Ref. 33. The values of the level density parameter, a, are given in Table III for all the relevant channels in the ^{20}Ne+^{12}C fusion. The spin cutoff parameter, $2\sigma^2$, is given by

$$2\sigma^2=(2\mathcal{I}_r/\hbar^2)t \ ,$$

where t is the nuclear temperature. The rigid body moment of inertia, $\mathcal{I}_r$, is calculated with the formula given by Davis and Nix[34] that takes into account the diffuseness corrections which are necessary for light systems. The radius parameter used with this formula was $r_0=1.3$ fm. The values of the level density parameter a were obtained by fitting the Fermi gas formula to the known levels for $A\leq 32$ taken from the compilation of Endt and Van der Leun.[35]

Figures 15 and 17 show the results of LILITA calculations using the above parameters and allowing for n, p, and α emission. Figure 16 shows the results for the Mg spectrum at $\theta_{lab}=5.4°$ and 13°. The solid histograms are the results of the Monte Carlo calculations for the uncorrelated emission of n's, p's, and α particles and they do not reproduce the high energy group at $\theta_{lab}=5.4°$ and the peaks labeled I and II at $\theta_{lab}=13°$. Within the context of the statistical model there is also some probability for emission of complex fragments such as Li or Be, and therefore a calculation for the ^{8}Be channel (the relevant one for the production of Mg) was done. All excited states of ^{8}Be up to 11 MeV were allowed to compete with n, p, and α emission, and the values for the Coulomb and centrifugal barriers (needed in the sharp cutoff approximation) for the ^{8}Be + ^{24}Mg channels were scaled simply by Z and $A^{1/3}$ dependence from the ones of the $\alpha+^{28}$Si channel. The level of ^{8}Be emission allowed for by the statistical model for compound nucleus decay, with these parameters, was too low to have any appreciable effect on the shape of the predicted energy spectra. In order to illustrate the kinematic features of such emission, the ^{8}Be yield has been arbitrarily increased by a factor of 5 with respect to that predicted by our statistical model calculations, and the results for the Mg spectra are shown by the dashed histograms in Fig. 16.

[1]For review articles of these phenomena see: H. Feshbach, J. Phys. (Paris) Colloq. C5, 177 (1976); articles by D. A. Bromley and by R. H. Siemssen in *Proceedings of International Conference on Molecular Phenomena, Hvar, Yugoslavia, 1977,* edited by N. Cindro (North-Holland, Amsterdam, 1978).

[2]J. V. Maher, M. W. Sachs, R. H. Siemssen, A. Weidinger, and D. A. Bromley, Phys. Rev. 188, 1665 (1969).

[3]J. J. Kolata, R. C. Fuller, R. M. Freeman, F. Haas, B. Heusch, and A. Gallman, Phys. Rev. C 16, 891 (1977); 19, 2237 (1979); I. Tserruya, Y. Eisen, D. Pelte, A. Gavron, H. Oeschler, D. Bernt, and H. L. Harney, *ibid.* 18, 1688 (1978).

[4]P. P. Singh, D. A. Sink, P. Schwandt, R. E. Malmin, and R. H. Siemssen, Phys. Rev. Lett. 28, 1714 (1972).

[5]R. Vandenbosch, M. P. Webb, and M. S. Zisman, Phys. Rev. Lett. 33, 842 (1974).

[6]R. G. Vandenbosch and K. G. Bernhardt, J. Phys. (Paris) Lett. 37, L161 (1976).

[7]H. Doubre, J. C. Roynette, E. Plagnol, J. M. Liseauz, P. Martin, and P. de Saintignon, Phys. Rev. C 17, 131 (1978).

[8]J. Menet, A. J. Cole, N. Longeueue, J. J. Lucas, G. Mariolopoulos, J. B. Viano, J. C. Saulnier, and D. H. Koang, J. Phys. 38, 1051 (1977).

[9]F. Osterfeld, V. Hzindo, and C. Toepffer, Phys. Lett. 68B, 319 (1977).

[10]F. Saint Laurent, M. Conjeaud, S. Harar, J. M. Loiseaux, J. Menet, and J. B. Viano, Nucl. Phys. A327, 517 (1979).

[11]I. Tserruya, J. Barrette, S. Kubono, P. Braun Munzinger, M. Gai, and C. D. Uhlhorn, Phys. Rev. C 21, 1864 (1980).

[12]P. Braun-Munzinger, G. M. Berkowitz, T. M. Cormier, C. M. Jachcinski, and J. W. Harris, Phys. Rev. Lett. 38, 944 (1977); S. Kubono, P. D. Bond, and C. E. Thorn, Phys. Lett. 81B, 140 (1979); J. Barrette, M. J. LeVine, P. Braun-Munzinger, G. M. Berkowitz, M. Gai, J. W. Harris, and C. M. Jachcinski, Phys. Rev. Lett. 40, 445 (1978); A. Roy, A. D. Frawley, and K. W. Kemper, Phys. Rev. C 20, 2143 (1979); R. Ost, M. R. Clover, R. M. DeVries, B. R. Fulton, H. E. Gove, and N. J. Rust, *ibid.* 19, 740 (1979); J. C. Peng, D. L. Hanson, J. D. Moses, O.W.B. Schult, Nelson Stein, J. W. Sunier, and N. Cindro, Phys. Rev. Lett. 42, 1458 (1979).

[13]J. C. Peng, J. V. Maher, M. S. Chiou, W. J. Jordan, F. C. Wang, and M. W. Wu, Phys. Lett. 80B, 35 (1978); M. Paul, S. J. Sanders, J. Cseh, D. F. Geesaman, W. Henning, D. G. Kovar, C. Olmer, and J. P. Schiffer, Phys. Rev. Lett. 40, 1310 (1978); C. K. Gelbke, T. Awes, and U. E. P. Berg, *ibid.* 41, 1778 (1978); S. M. Lee, J. C. Adloff, P. Chevallier, D. Disdier, V. Rauch, and F. Scheibling, *ibid.* 42, 429 (1979).

[14]J. L. C. Ford, Jr., J. Gomez del Campo, S. Shapira, M. R. Clover, R. M. DeVries, B. R. Fulton, R. Ost, and C. F. Maguire, Phys. Lett. 89B, 48 (1979).

[15]D. Shapira, J. L. C. Ford, Jr., J. Gomez del Campo, R. G. Stokstad, and R. M. DeVries, Phys. Rev. Lett. 43, 1781 (1979).

[16]R. G. Stokstad, A. H. Snell, and D. C. Hensley, Nucl. Instrum. Methods 141, 499 (1977).

[17]J. Gomez del Campo, R. G. Stokstad, J. A. Biggerstaff, R. A. Dayras, A. H. Snell, and P. H. Stelson, Phys. Rev. C 19, 2170 (1979).

[18]J. Wilczynski, Phys. Lett. 47B, 484 (1973).

[19]T. M. Cormier, P. Braun-Munzinger, P. M. Cormier, J. W. Harris, and L. L. Lee, Jr., Phys. Rev. C 16, 215 (1977).

[20]P. Braun-Munzinger, T. M. Cormier, and C. K. Gelbke, Phys. Rev. Lett. 37, 1582 (1976).

[21]R. R. Betts and S. B. Cicenzo, Phys. Rev. C 19, 2070 (1979).

[22]J. B. Natowitz, M. N. Namboodiri, R. Eggers, P. Gonthier, K. Geoffroy, R. Hanus, C. Towsley, and K. Das, Nucl. Phys. A277, 477 (1977).

[23]D. Pelte and U. Smilansky, Phys. Rev. C 19, 2196 (1979).

[24]R. A. Broglia, O. Civitarese, C. H. Dasso, and A. Winther, Phys. Lett. 73B, 405 (1978); R. A. Broglia, C. H. Dasso, G. Pollarolo, and A. Winther, Phys. Rev. Lett. 40, 707 (1978).

[25]D. Pelte, U. Winkler, R. Novotny and H. Graf, Nucl. Phys. A371, 455 (1981).

[26]D. Shapira, D. DiGregorio, J. Gomez del Campo, R. A. Dayras, J. L. C. Ford, Jr., A. H. Snell, P. H. Stelson, R. G. Stokstad, and F. Pougheon, Phys. Rev. C (to be published).

[27]J. Gomez del Campo and R. G. Stokstad, Oak Ridge National Laboratory Report ORNL TM-7295, 1981.

[28]N. Austern, *Direct Nuclear Reaction Theories* (Wiley, New York, 1970), pp. 115–129.

[29]A. Gobbi, R. Wieland, L. Chua, D. Shapira, and D. A. Bromley, Phys. Rev. C 7, 301 (1973).

[30]D. G. Kovar, D. F. Geesaman, T. H. Braid, Y. Eisen, W. Henning, T. R. Ophel, M. Paul, K. E. Rehm, S. J. Sanders, P. Sperr, J. P. Schiffer, S. L. Tabor, S. Vigdor, B. Zeidman, and F. W. Prosser, Jr., Phys. Rev. C 20, 1305 (1979).

[31]M. E. Ortiz, J. Gomez del Campo, Y. D. Chan, D. E. DiGregorio, J. L. C. Ford, D. Shapira, R. G. Stokstad, J. P. F. Sellschop, R. Parks, and D. Weiser, Phys. Rev. C 25, 1436 (1982).

[32]C. M. Perey and F. G. Perey, Nuclear Data, Sect. B 10, 539 (1972).

[33]A. Gilbert and A. G. W. Cameron, Can. J. Phys. 43, 1446 (1965).

[34]K. T. R. Davies and R. Nix, Phys. Rev. C 14, 1977 (1976).

[35]P. M. Endt and C. Van der Leun, Nucl. Phys. A214, 1 (1973).